

Photon Conversion and Interaction in a Quasi-Phase-Matched Microresonator

Jia-Yang Chen^{1,2,*†} Zhan Li,^{1,2,*} Zhaojun Ma^{1,2} Chao Tang,^{1,2} Heng Fan,^{1,2} Yong Meng Sua,^{1,2} and Yu-Ping Huang^{1,2,‡}

¹*Department of Physics, Stevens Institute of Technology, 1 Castle Point Terrace, Hoboken, New Jersey 07030, USA*

²*Center for Quantum Science and Engineering, Stevens Institute of Technology, 1 Castle Point Terrace, Hoboken, New Jersey 07030, USA*

(Received 3 June 2021; revised 12 October 2021; accepted 11 November 2021; published 1 December 2021)

The conversion and interaction between quantum signals at the single-photon level are essential for scalable quantum photonic information technology. Using a fully optimized periodically poled lithium niobate microresonator, we demonstrate ultraefficient sum-frequency generation on a chip. The external quantum efficiency reaches $(65 \pm 3)\%$ with only $(104 \pm 4)\text{-}\mu\text{W}$ pump power. At peak conversion, 3×10^{-5} -noise photon is created during the cavity lifetime, which meets the requirement of quantum applications using single-photon pulses. Using a pump and signal in single-photon coherent states, we directly measure the conversion probability produced by a single pump photon to be 10^{-5} , which is a significant improvement from the state of the art, and the photon-photon coupling strength to be 9.1 MHz. Our results mark steady progress toward quantum nonlinear optics at the ultimate single-photon limit, with potential applications in highly integrated photonics and quantum optical computing.

DOI: 10.1103/PhysRevApplied.16.064004

I. INTRODUCTION

Unlike electrons, atoms, or any other material particles, photons do not interact with each other in a vacuum. Even when mixed in optical media of the best-known nonlinearities, their interaction is so weak that high optical intensities are needed to produce an appreciable effect. This inefficiency accounts for significant difficulties facing practical implementations of quantum transduction [1], faithful entanglement swapping [2,3], and heralded entanglement generation [4,5], to name a few. It also prohibits the construction of nonlinear photon-photon gates, thus forming a bottleneck for the development of scalable quantum computers at room temperature [6].

Recent advances in nanophotonics bring hope to overcome this challenge, by providing tight optical confinement, strong mode overlap, and extended interaction length. Encouragingly, optical processes with improved efficiency are demonstrated in nanophotonic circuits made of silicon nitride [7,8], aluminum nitride [9], gallium arsenide [10], gallium phosphide [11], aluminum gallium arsenide [12], and lithium niobate [13,14]. Among various candidates, thin-film lithium niobate (TFLN) on an insulator has quickly arisen to a material platform of

choice, due to its favorable ferroelectricity, wide optical transparency window, strong second-order nonlinearity $\chi^{(2)}$, and outstanding electro-optical responses. Compared with third-order nonlinear [$\chi^{(3)}$] materials, TFLN is centroasymmetric and possesses exceptionally large second-order nonlinearity [$\chi^{(2)}$] to produce orders of magnitude stronger effects, which is desirable for optical nonlinearities at the single-photon level. Thus far, a variety of TFLN microresonators have been demonstrated with impressive nonlinearities [13–18]. However, their performance is capped by the use of relatively small $\chi^{(2)}$ susceptibilities (e.g., $d_{31} \sim 4.7 \text{ pm/V}$) [15], poor mode overlapping [16,18], and/or low photon-extraction efficiency [13,15–17]. For photon conversion and interaction, while their high efficiency is predicted from, e.g., second-harmonic generation (SHG) [15–17] or parametric down-conversion experiments [13], there has been no direct demonstration.

Here, we present a TFLN resonator that overcomes the aforementioned shortcomings and delivers its promised high efficiency for photon conversion and interaction. As illustrated in Fig. 1(a), it is an overly coupled triply resonant periodically poled lithium niobate (PPLN) microresonator for sum-frequency generation (SFG). All interacting light waves are in the low-loss fundamental modes with nearly perfect overlap and interact through TFLN's largest $\chi^{(2)}$ susceptibility tensor element (e.g., $d_{33} \sim 27 \text{ pm/V}$). It achieves an impressive photon-photon coupling strength of $g = 9.1 \text{ MHz}$ (angular frequency). Crucially, by strongly overcoupling the cavity, to minimize

*J.-Y. Chen and Z. Li contributed equally to this work.

†jchen59@stevens.edu

‡yhuang5@stevens.edu

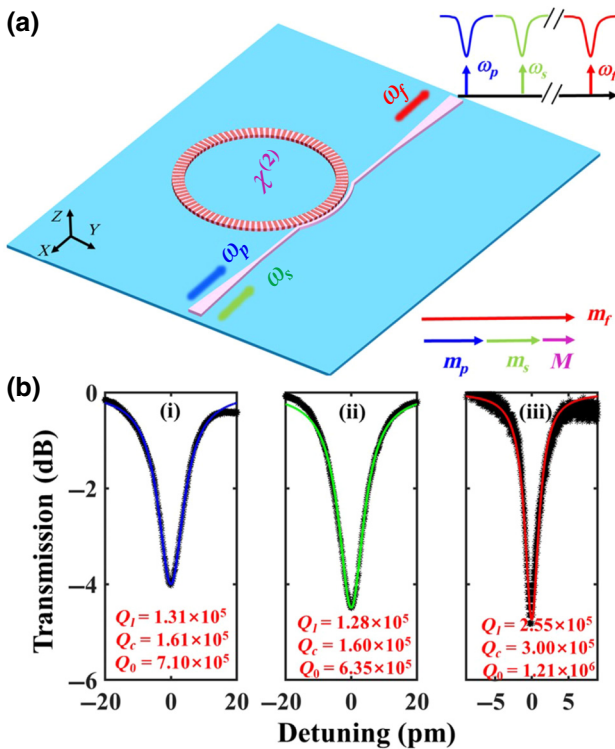


FIG. 1. Integrated TFLN circuits for photon conversion and interaction. Schematic of the Z-cut periodically poled microring, where the pump, ω_p , and signal, ω_s , couple into the microring and generate SF light, ω_f , via a $\chi^{(2)}$ process. Pulley coupler is designed for overcoupling all light waves, for high photon-extraction efficiency. Insets illustrate triply resonant and quasi-phase-matching conditions. (b) Optical spectra of interacting TM_{00} cavity modes at (i) 1560.15 nm, (ii) 1551.85 nm, and (iii) 778.00 nm.

the extraction loss of the sum-frequency (SF) photons, we demonstrate photon conversion at an external efficiency of 65% with only about 100- μW pump power, marking orders of magnitude improvement over the state of the art across various existing photonic platforms (see Table I). At peak conversion, the on-chip noise photon flux is only 3×10^{-5} photons per 100-ps cavity lifetime, despite small detuning pumping. This ultrahigh external efficiency, yet low noise, creates opportunities in various applications, like quantum-frequency conversion, optical squeezing, and phase-sensitive amplification.

In addition to the large coupling strength, our device's high cavity quality for all interacting waves provides an extended interaction length to boost optical nonlinearities towards the single-photon regime. To assess this prospect, we further investigate photon interactions between two single-photon signals in weakly coherent states. Our measurement directly shows that, with only one pump photon in the microring, the external quantum efficiency for signal photon conversion is about 10^{-5} , which is higher than the previously reported value of 10^{-7} [20].

As a whole, our results constitute progress in the long pursuit of nonlinear optics in its ultimate quantum limit, where a single photon is enough to produce significant nonlinear effects. While there is still a significant journey to take before hitting the finish line, the fact that we can attain the theoretical performance of this device is critical for us to take steps forward. By further improving the cavity quality, strong photon-photon interactions are within sight. Based on the current nonlinear parameters, a cavity quality factor of 10^8 , which has been demonstrated in lithium niobate microdisks [18], will enable CNOT gate between single photons. Meanwhile, the demonstrated photon-conversion and -interaction efficiency can already elevate the performance of nonlinear optical devices for heralded entanglement generation, faithful entanglement swapping, and so on.

II. DEVICE DESIGN AND CHARACTERIZATION

In the $\chi^{(2)}$ cavity, the effective Hamiltonian describing SFG between photons in their single modes is

$$\hat{H}_{\text{eff}} = \hbar g(\hat{a}_p \hat{a}_s \hat{a}_f^\dagger + \hat{a}_p^\dagger \hat{a}_s^\dagger \hat{a}_f), \quad (1)$$

where $\{\hat{a}_j\}$ are the annihilation operators with $j = p, s$, and f representing the pump, signal, and SF light, respectively, each with angular frequency ω_j . g is the photon-photon coupling strength, which can be interpreted as the effective Rabi frequency produced by a pump photon (see Appendixes A and B). It is given by

$$g \propto \frac{d_{\text{eff}} \xi}{\sqrt{V_{\text{eff}}}} \delta(m_f - m_p - m_s - M), \quad (2)$$

where d_{eff} is the effective nonlinear susceptibility. ξ is the mode-overlapping factor. V_{eff} is the effective mode volume. m_j is the azimuthal order of the cavity modes, and M is the azimuthal-poling-grating number, so that $\delta(m_f - m_p - m_s - M)$ accounts for quasi-phase matching (QPM) by periodic poling. The optimization procedure of the device and details of device fabrication are presented in Appendix A.

The fiber-chip-fiber coupling losses of the device are measured to be (8 ± 0.15) dB at 1556 nm and (9.5 ± 0.2) dB at 778 nm. To find phase matching, we first search for strong SHG across the C band by sweeping an infrared laser while optimizing the chip's temperature. This gives several cavity modes around 1556 nm, based on which we select a set of cavity modes at 1560.15, 1551.85, and 778.00 nm, considering the overcoupling requirement and limited by our visible band-pass filter (BPF, bandwidth ~ 3 nm, 760–780 nm). To reduce the Raman background, we designate the 1560.15-nm mode to the pump. For this set, $m_p = 602$, $m_s = 606$, and $m_f = 1357$, so that $M = 149$. The loaded quality factors, $Q_{j,l}$, are measured for

TABLE I. Overview of state-of-the-art frequency conversion in $\chi^{(2)}$ and $\chi^{(3)}$ cavities. η_{con} , conversion efficiency as the ratio of optical powers (P_s/P_p); η_{QE} , quantum efficiency as the ratio of photon numbers (N_f/N_s); FWM BS, four-wave mixing Bragg scattering; DFWM, degenerate four-wave mixing. Q_l lists the loaded quality factors for the pump, signal, and SF waves in the case of FWM BS, DFWM, and SFG, and the pump and second-harmonic waves in the case of SHG.

Material platform	Structure	Nonlinear process	$Q_l (\times 10^5)$	$\eta_{\text{con}} (\%)$	$\eta_{\text{QE}} (\%)$	Pump power (mW)	Ref.
Si ₃ N ₄	Microring	FWM BS	1.5, 1.5, 2.4	...	60	50, 8	[7]
Si ₃ N ₄	Microring	DFWM	2.8, 3.0, 1.2	30	...	0.33	[8]
AlN	Microring	SFG	3.0, 3.0, 1.4	...	42	35	[9]
PPLN	Microring	SHG	1.3, 3.0	20	...	0.3	[13]
PPLN	Microring	SHG	1.5, 0.6	52	...	1.8	[14]
PPLN	Microring	SHG	8, 1.8	15	...	0.115	[15]
PPLN	Microdisk	SHG	750, ...	66	...	0.11	[18]
PPLN	Millimeter disk	SHG	120, 80	36	...	9	[19]
PPLN	Microring	SFG	1.3, 1.3, 2.6	...	65	0.1	This work

each mode, while the coupling, $Q_{j,c}$, and intrinsic, $Q_{j,0}$, factors are calculated by fitting the resonance spectra, as shown in Fig. 1(b). These Q values, according to Eqs. (A1)–(A2), give the highest possible external quantum efficiency of $\eta_{\text{QE}}^{\text{max}} \approx 65\%$. For an even higher efficiency, the cavity needs to be further overcoupled.

III. LOW-NOISE FREQUENCY CONVERSION

We perform SFG using the setup detailed in Appendix C. We first couple a strong pump at 1560 nm and a weak signal at 1552 nm into the microring, and fine-tune the microring temperature and laser wavelengths to verify QPM and triple resonance. The resulting spectrum, measured without any filtering, thus manifesting all possible nonlinear processes, is shown in Fig. 2. It exhibits a clean profile with a low baseline, except for a residual second-harmonic peak at about 780 nm for the strong pump. This peak is only significant in the high-conversion regime (i.e., $> 50\%$) and can be conveniently filtered out. In this experiment, we reject it using an approximately 3-nm band-pass filter centered at 778 nm. The otherwise low background over the entire spectral range shows that all other competing processes are well suppressed, which is desirable for quantum applications.

In this experiment, the signal power is fixed to be about 37 nW on a chip, while the pump power is gradually increased. During the measurement, we need only to slightly optimize the temperature within $(45 \pm 0.3)^\circ\text{C}$ and tune the wavelengths of both lasers within ± 20 pm to compensate for slight phase mismatch and resonance drift caused by thermo-optical and photorefractive effects [14]. The quantum efficiency as a function of the on-chip pump power is shown in Fig. 3. Thanks to the overcoupling and nearly ideal poling, $(65 \pm 3)\%$ quantum efficiency is achieved with $(104 \pm 4)\text{-}\mu\text{W}$ pump power. Taking into account all insertion losses both on and off the chip, this corresponds to about 9% total efficiency. In the low-conversion region, the normalized power-transduction efficiency is fitted to be about $4.5\% \mu\text{W}^{-1}$. By fitting experimental data with the steady-state solutions to Eqs. (B1)–(B3), as shown in Fig. 3, the photon-photon coupling coefficient, g , is determined to be 8.2 MHz.

The above results speak to the ultrahigh efficiency. For quantum-frequency conversion, it is critical that no significant in-band noise is injected during conversion. There are multiple processes that can produce in-band noise, such as Raman scattering from a strong classical pump to the signal band followed by SFG, Raman scattering by the pump's residual SH light, and spontaneous

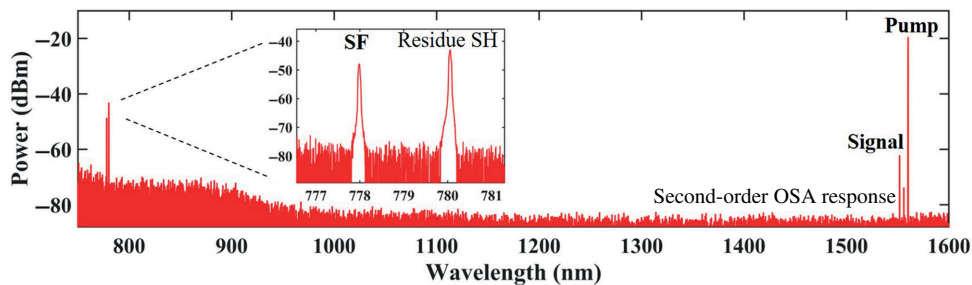


FIG. 2. Original optical spectrum before any optical filtering when strong pump and weak signal are applied. In high-conversion region, signal starts to be depleted. Inset shows magnified spectrum around the SF band. After correcting for coupling loss, on-chip powers of pump, signal, and SF waves are -13.8 , -44.3 , and -44.0 dBm, respectively.

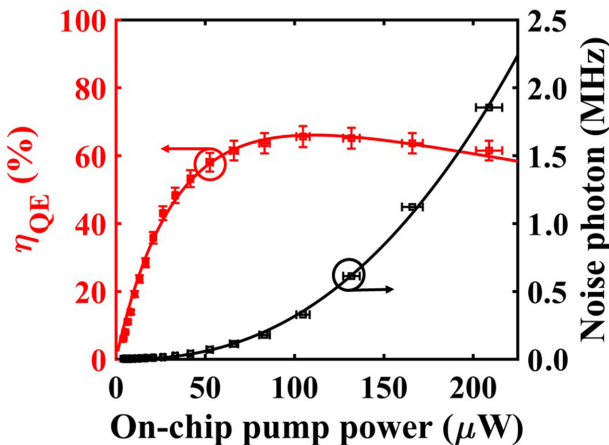


FIG. 3. Quantum efficiency, η_{QE} (left axis, red squares), and noise photon flux, N_{noise} (right axis, black squares), plotted against on-chip pump power. $\eta_{QE} = 65\%$ is obtained at pump power around $100 \mu\text{W}$. Error bars for left axis and x axis are estimated according to coupling instability. Error bars of noise photon on right axis are estimated by uncertainty assuming Poissonian photon-counting statistics.

parametric down-conversion (SPDC) followed by SHG and SFG. To quantify their total contributions, we measure the noise photon flux generated in the SF band when only the pump is applied. To ensure total rejection of any out-band noise, the SF photons are passed through additional free-space filters (see Appendix C), before being detected by a silicon-based single-photon detector (Si SPD; quantum efficiency, 50%; dark count, 250 Hz). The results are plotted in Fig. 3, where the increase of the noise photon flux is between quadratic and cubic with the pump power. This result indicates that, besides Raman scattering, the cascaded SPDC and SFG processes are also present, similar to what we observe in a PPLN nanowaveguide [21]. At the 65% peak QE, the on-chip noise photon flux is 0.3 MHz under continuous-wave pumping. If using approximately 100-ps pulses that match the cavity lifetime, the noise photon per pulse is 3×10^{-5} , which is low, especially given the small detuning between the pump and signal that are both in the telecom C band. This noise level can be substantially lowered by, for example, further detuning the pump from the signal [22].

IV. INTERACTION BETWEEN PHOTON-LEVEL COHERENT STATES

Strong interactions between single photons are of great value for both fundamental optics studies and quantum applications, such as faithful quantum-entanglement swapping [2,3], heralded-entanglement source [4,5], and device-independent quantum-key distribution [23]. Here, we characterize the device responses in the single-photon

regime by attenuating the pump and signal to weak coherent states at the single-photon level. Their photon fluxes are carefully monitored by two superconducting single-photon detectors (SNSPDs, see Appendix C).

To maximize the detection efficiency for SF photons, we remove the free-space filtering system, which is used in the last section to reject background noise created by the strong pump, and directly couple the SF photons from the chip to the Si SPD via a lensed fiber. To ensure that the pump photons do not generate background counts (which could contribute to the overestimation of single-photon nonlinearity), we block the signal and verify that, even at the highest on-chip flux ($\sim 5 \text{ GHz}$), the photon counts remain at the dark-count level ($\sim 250 \text{ Hz}$). Here, the total detection efficiency for the sum-frequency photons is $\eta = \eta_d \eta_c \approx 17\%$, with a detector efficiency of $\eta_d \sim 50\%$ and a coupling efficiency of $\eta_c \sim 33.5\%$.

The measurement results are shown in Fig. 4, where we observe a linear dependency of the quantum efficiency on the intracavity pump-photon number. The on-chip quantum efficiency is about 10^{-5} when there is one pump photon, on average, in the cavity, after correcting for coupling loss and finite detector efficiency. By fitting with the coupling-mode equations, we extract the photon-photon coupling coefficient, g , to be 9.1 MHz, compared to 8.2 MHz from the classical measurement. This slightly higher value may come from better QPM or triple resonance for single-photon light waves, due to the absence of thermo-optical and photorefractive effects.

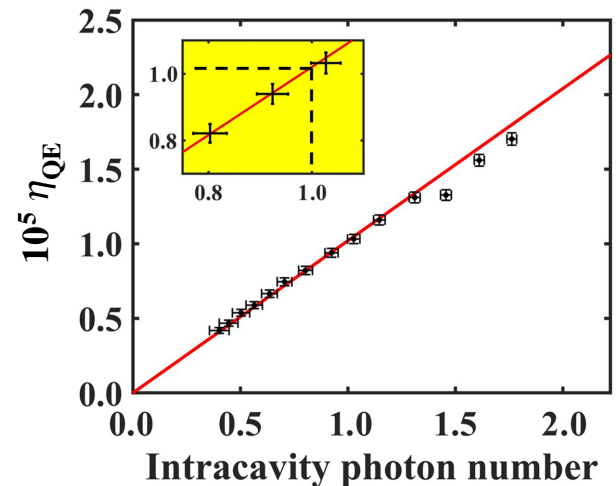


FIG. 4. Quantum efficiency, η_{QE} , versus intracavity mean pump-photon number. Inset is a magnification to show that a quantum efficiency of $\eta_{QE} = 10^{-5}$ is achieved at one intracavity pump photon (corresponding to photon flux $N_p = 2.8 \text{ GHz}$), where the intracavity signal photon number is fixed at 0.25 (corresponding to photon flux $N_s = 0.7 \text{ GHz}$). All error bars are estimated assuming Poissonian photon-counting statistics.

V. CONCLUSIONS

We demonstrate photon conversion and interaction with high efficiency and low noise in a Z -cut periodically poled microring on thin-film lithium niobate. Combining nearly perfect QPM, tight mode confinement, high cavity quality, and efficient photon extraction, we achieve 65% wavelength transduction with only about $100\text{-}\mu\text{W}$ pump power, advancing the state of the art. Despite a small detuning between the signal and pump, at peak conversion, only 3×10^{-5} noise photons are created over the cavity lifetime, thanks to the deep single-mode condition and suppression of side processes. The same device allows nonlinear interactions between two single-photon-level coherent states, where the photon-photon coupling strength reaches 9.1 MHz, and a single photon can produce 0.01 internal Rabi rotation angle (see Appendix B). The external quantum efficiency is directly measured to be about 10^{-5} , in comparison with a reported efficiency of 10^{-7} . Our results mark steady progress towards quantum nonlinear optics in the single-photon regime, with broad implications in areas of fundamental studies and applied quantum-information technology. Additionally, the demonstrated photon conversion and interaction are ready to be integrated with other passive and active elements on the same chip, such as PPLN waveguides [24,25], electro-optical modulators [26], frequency-comb sources [27–30], and microring filters [31], to create functional quantum devices with practical impacts [32]. Thus, a superior platform of photonic integrated circuits is within sight for scalable quantum applications.

ACKNOWLEDGMENTS

The research is supported, in part, by the National Science Foundation (Grants No. 1641094, No. 1842680, and No. 1806523) and the National Aeronautics and Space Administration (Grant No. 80NSSC19K1618). Device fabrication is performed at the Nanofabrication Facility of the Advanced Science Research Center (ASRC), City University of New York (CUNY).

APPENDIX A: DEVICE DESIGN AND FABRICATION

In this work, we use a microring with a radius of $80\text{ }\mu\text{m}$ and a cross section of 600 nm in height and 1700 nm in top width. The pump and signal are both in the telecom C band and their SF is in the visible band, which is chosen with repeater-based quantum communications in mind. To maximize g , all three waves are in the fundamental quasi-transverse-magnetic (quasi-TM) modes and interact through TFLN's largest nonlinear tensor, d_{33} , with over 90% mode overlap. As shown in Fig. 5, concentric periodic poling is applied to the microring for QPM.

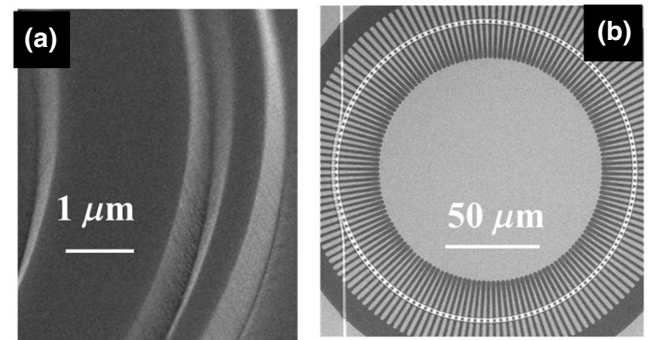


FIG. 5. (a),(b) SEM images of etched pulley coupler before poling process and periodic poled microring after removing poling electrodes, respectively.

To ensure triple resonances for all waves, fine temperature tuning ($\sim 0.01^\circ\text{C}$) is applied to compensate for any resonant mismatch due to any fabrication error.

For photon conversion and interaction, the device's figure of merit is the external quantum efficiency (QE), which is defined as

$$\eta_{\text{QE}} = \frac{N_f}{N_s}, \quad (\text{A1})$$

where N_s is the number of input-signal photons to the cavity and N_f is that of converted SF photons at the cavity output (thus accounting for any internal cavity loss). This is in contrast to previous demonstrations, where critical coupling is adopted to maximize the intracavity optical power for high conversion efficiency [13,15–17]. However, most of the input power and about half of the converted photons are lost inside the cavity, rendering a rather low QE while prohibiting cascaded operations. For practical applications, one instead needs to overcouple the cavity, so that photons can be extracted before they are significantly lost in the cavity.

Under QPM and triple resonance, the maximum QE is given by [33]

$$\eta_{\text{QE}}^{\max} \approx \frac{Q_{s,l} Q_{f,l}}{Q_{s,c} Q_{f,c}}, \quad (\text{A2})$$

where $Q_{j,o}$ is the quality factor, with $o = c, l$ denoting the coupling and loaded Q , respectively. It is reached with an optimal pump power of

$$P_p^{\text{opt}} \approx 8 \frac{\eta_{\text{QE}}^{\max}}{\eta_{\text{tran}}^{\text{nor}}}, \quad (\text{A3})$$

where $\eta_{\text{tran}}^{\text{nor}} = P_f / (P_s P_p)$ is the normalized power transduction efficiency, with P_j as the optical power of the j th wave. In our case, $\eta_{\text{QE}}^{\max} \approx 65\%$ and $\eta_{\text{tran}}^{\text{nor}} \approx 4.5\%/\mu\text{W}$, so that the optimal power is around $115\text{ }\mu\text{W}$.

We use a pulley coupler with optimized dimensions to achieve proper overcoupling for both the signal and SF modes. This is done by first determining its top width by requiring $n_p R_p = n_r R_r$ [34], where $n_{p,r}$ are the effective refractive indices of the pulley waveguide and microring modes, respectively, for the sum-frequency wave, and R_p and R_r denote their radii. For the SF wave, the waveguide-microring coupling strength is proportional to the length of the pulley coupler and inversely proportional to their gap. For the signal mode, in contrast, the coupling strength varies by $\text{sinc}(\Delta\Phi)$, where $\Delta\Phi$ is the coupling-phase mismatch. This allows us to carefully design the dimensions to create the desirable overcoupling for both signal and sum-frequency waves.

APPENDIX B: COUPLED-MODE THEORY

The dynamics of SFG inside the $\chi^{(2)}$ cavity, neglecting Rayleigh backscattering and assuming the single-mode condition, is governed by the following coupled-mode equations:

$$\frac{da_p}{dt} = \left(i\delta_p - \frac{\kappa_{p,t}}{2} \right) a_p - ig^* a_s^* a_f - i\sqrt{\kappa_{p,c}} F_p, \quad (\text{B1})$$

$$\frac{da_s}{dt} = \left(i\delta_s - \frac{\kappa_{s,t}}{2} \right) a_s - ig^* a_p^* a_f - i\sqrt{\kappa_{s,c}} F_s, \quad (\text{B2})$$

$$\frac{da_f}{dt} = \left(i(\delta_p + \delta_s + \Delta\omega) - \frac{\kappa_{f,t}}{2} \right) a_f - ig a_p a_s, \quad (\text{B3})$$

where $\kappa_{j,o} = \omega_j / Q_{j,o}$ are the cavity dissipation rates; $Q_{j,o}$ are the quality factors of the cavity mode; ω_j is the angular frequency, with $j = p, s$, and f indicating the pump, signal, and sum-frequency modes, respectively, and $o = 0, c$, and t denoting intrinsic, coupling, and total dissipation rates, with $\kappa_t = \kappa_0 + \kappa_c$. $\delta_j = \omega_j - \omega_{j,0}$ is the laser-cavity detuning and $\omega_{j,0}$ is the cavity resonance; $F_j = \sqrt{N_j}$, where N_j is the photon number. Because of energy conservation in a parametric conversion process, $\omega_f = \omega_p + \omega_s$ permits $\delta_p + \omega_{p,0} + \delta_s + \omega_{s,0} = \delta_f + \omega_{f,0}$, and thus, $\delta_f = \delta_p + \delta_s + \Delta\omega$, where $\Delta\omega = \omega_{p,0} + \omega_{s,0} - \omega_{f,0} \approx 0$, when it is a triply resonant cavity. The photon-photon coupling coefficient, g , is given by

$$g = \sqrt{\frac{\hbar\omega_p\omega_s\omega_f}{2\epsilon_0\epsilon_p\epsilon_s\epsilon_f}} \frac{\frac{2}{\pi}d_{\text{eff}}\xi}{\sqrt{A_{\text{eff}}2\pi R}} \delta(m_f - m_p - m_s - M), \quad (\text{B4})$$

$$\xi = \frac{\iint E_f^* E_p E_s dx dy}{(\iint |E_p|^2 dx dy \iint |E_s|^2 dx dy \iint |E_f|^2 dx dy)^{1/3}}, \quad (\text{B5})$$

where ϵ_0 is the vacuum permittivity; $\epsilon_j = n_j^2$ are the relative permittivities, with n_j giving the effective refractive indices; d_{eff} is the effective nonlinear susceptibility; ξ is the mode-overlapping factor; and V_{eff} is the effective mode volume. m_j are the azimuthal orders of the cavity modes; M is the azimuthal-poling-grating number. For the quasi-phase-matched case, $m_f - m_p - m_s - M = 0$.

At steady state, the output field of SF is defined as $b_f = i\sqrt{\kappa_{f,c}} a_f$ and the quantum efficiency of photon conversion is given by $\eta_{\text{QE}} = N_f / N_s = |b_f|^2 / N_s$. The intracavity pump and signal photon number are given by $|a_p|^2$ and $|a_s|^2$, respectively. The above quantum efficiency gives the probability of a signal photon at the cavity input being converted into its sum frequency and appearing at the cavity output. It has accounted for signal coupling loss and SF extraction loss. It is thus a direct measure of the device's figure of merit, which dictates its performance in applications.

Another measure, of less practical relevance but nonetheless describing an intrinsic property, is the internal Rabi rotation angle, $\theta = 2gQ_{p,i}/\omega_p$. That is, Eq. (1) can be interpreted as the pump-induced Rabi oscillation between signal and SF photons. θ then gives how much Rabi rotation a pump photon induces during it being lost in the cavity. In our case, $g = 9.1 \times 10^6$ and $Q_{p,i} = 7.1 \times 10^5$, so that $\theta = 0.01$, which is already appreciable from a fundamental standpoint. Increasing θ to $\pi/2$ would require improving $Q_{p,i}$ to 10^8 , which has been demonstrated in polished TFLN microdisks [18].

We implement the time-split step method to numerically solve the coupled-mode equations. The parameters used in the simulation for Figs. 3 and 4 are listed in Table II.

APPENDIX C: EXPERIMENTAL SETUP

We use the setup shown in Fig. 6 to characterize the device and perform the photon-conversion and -interaction experiment. The whole chip is placed on a thermoelectric cooler and the temperature is set to about 45 °C. For linear characterization, as shown in Fig. 6(a), we use two polarized tunable continuous-wave (cw) lasers (Santec 550 and Newport TLB-6712) and tapered fibers (OZ OPTICS) to independently characterize the fiber-chip-fiber coupling, the losses of which are measured to be (8 ± 0.15) dB at around 1556 nm and (9.5 ± 0.2) dB at around 778 nm, respectively. For its nonlinear optical properties, we sweep the infrared laser across the whole C band while optimizing the chip's temperature to achieve strong SHG.

Once we identify the quasi-phase-matching resonances, we switch to the setup in Fig. 6(b) for sum-frequency generation. An additional tunable cw laser (Coherent, MTP-1000) is used to serve as the signal. We further optimize the system around its optimum SHG condition to maximize the SFG.

TABLE II. Simulation parameters used in coupled-mode equations models for sum-frequency generation.

Parameter	Description	Value	Unit
$\kappa_{p,t}$	Total dissipation rate of pump mode	1467.9	MHz ($\times 2\pi$)
$\kappa_{p,0}$	Intrinsic dissipation rate of pump mode	270.8	MHz ($\times 2\pi$)
$\kappa_{p,c}$	Coupling dissipation rate of pump mode	1197.0	MHz ($\times 2\pi$)
$\kappa_{s,t}$	Total dissipation rate of signal mode	1510.3	MHz ($\times 2\pi$)
$\kappa_{s,0}$	Intrinsic dissipation rate of signal mode	304.4	MHz ($\times 2\pi$)
$\kappa_{s,c}$	Coupling dissipation rate of signal mode	1205.9	MHz ($\times 2\pi$)
$\kappa_{f,t}$	Total dissipation rate of sum-frequency mode	1512.2	MHz ($\times 2\pi$)
$\kappa_{f,0}$	Intrinsic dissipation rate of sum-frequency mode	318.7	MHz ($\times 2\pi$)
$\kappa_{f,c}$	Coupling dissipation rate of sum-frequency mode	1193.5	MHz ($\times 2\pi$)
d_{eff}^a	Effective nonlinear susceptibility	16.4	pm/V
d_{eff}^b	Effective nonlinear susceptibility	18.2	pm/V
A_{eff}	Effective mode area	1.0	μm^2
R	Radius of the microring	80	μm
ξ	Mode-overlapping factor	90	%

^aUsed in Fig. 3; fitted g is 8.2 MHz. ^bUsed in Fig. 4; fitted g is 9.1 MHz.

- (a) For classical measurements, an optical spectrum analyzer (OSA, Yokogawa AQ6370D) is used to collect data.
- (b) For quantum noise measurements, a silicon-based single-photon detector (Excelitas, efficiency 50%, dark count 250 Hz) and a free-space filtering system are introduced. These consist of two fiber collimators (insertion loss, IL \sim 2 dB); one short-pass filter (IL \sim 0.5 dB; extinction ratio, ER \sim 50 dB) and one band-pass filter (10 nm, 780 nm, IL \sim 0.5 dB, ER \sim 50 dB), rejecting the pump and signal in the C band while passing

through visible light; and three narrow-band-pass filters (Alluxa, 3 nm, IL \sim 1 dB, ER $>$ 120 dB), rejecting residual second-harmonic light of 780 nm while passing through the target light of 778 nm.

(c) For interactions between single-photon coherent states, a superconducting nanowire single-photon detector (ID Quantique, ID281, efficiency 85%, dark count 100 Hz) is used to monitor the input-photon flux. Due to the limited photon-count saturation rate (\sim 20 MHz) of SNSPDs, each monitoring channel has about 50 dB attenuation. Meanwhile, the free-space filtering system is removed to reduce

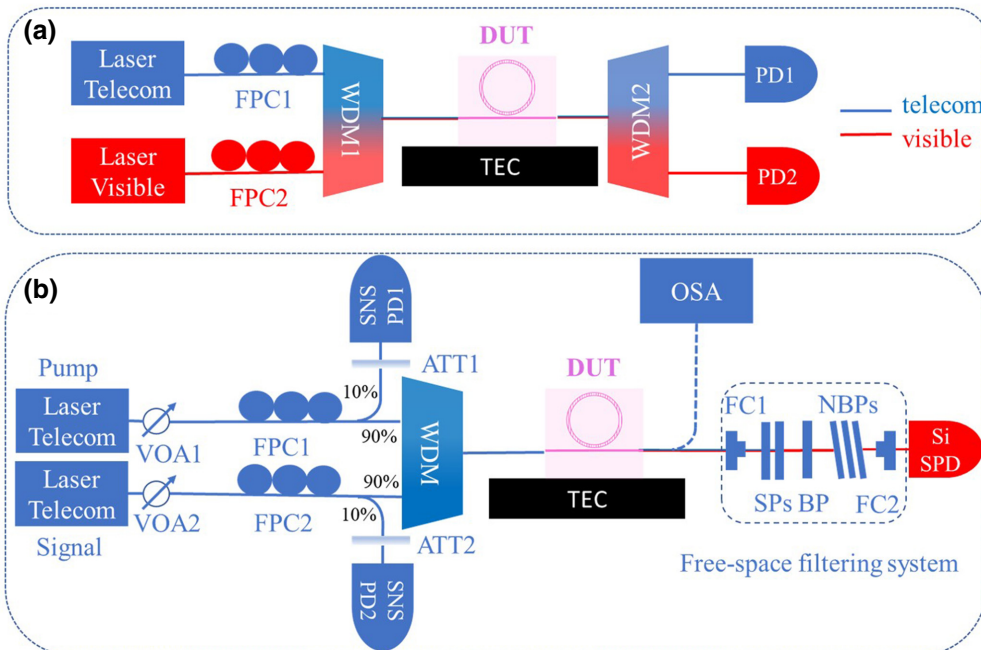


FIG. 6. Setups for classical (a) and quantum (b) experiments. Blue and red lines denote the telecom light path and visible path, respectively. FPC, fiber-polarization controller; TEC, thermoelectric cooler; WDM, wavelength-division multiplexing module; PD, photodetector; DUT, device under test; VOA, variable optical attenuator; ATT, optical attenuator; FC, fiber collimator; SP, short-pass filter; BP, band-pass filter; NBP, narrow-band-pass filter.

insertion loss ($\text{IL} \sim 4$ dB). The SF photons are directly measured by a silicon-based single-photon detector via a lensed fiber.

-
- [1] N. Maring, D. Lago-Rivera, A. Lenhard, G. Heinze, and H. de Riedmatten, Quantum frequency conversion of memory-compatible single photons from 606 nm to the telecom c-band, *Optica* **5**, 507 (2018).
- [2] N. Sangouard, B. Sanguinetti, N. Curtz, N. Gisin, R. Thew, and H. Zbinden, Faithful Entanglement Swapping Based on Sum-Frequency Generation, *Phys. Rev. Lett.* **106**, 120403 (2011).
- [3] Y. Li, Y. Huang, T. Xiang, Y. Nie, M. Sang, L. Yuan, and X. Chen, Multiuser Time-Energy Entanglement Swapping Based on Dense Wavelength Division Multiplexed and Sum-Frequency Generation, *Phys. Rev. Lett.* **123**, 250505 (2019).
- [4] C. Wagenknecht, C.-M. Li, A. Reingruber, X.-H. Bao, A. Goebel, Y.-A. Chen, Q. Zhang, K. Chen, and J.-W. Pan, Experimental demonstration of a heralded entanglement source, *Nat. Photonics* **4**, 549 (2010).
- [5] S. Barz, G. Cronenberg, A. Zeilinger, and P. Walther, Herald-ed generation of entangled photon pairs, *Nat. Photonics* **4**, 553 (2010).
- [6] D. E. Chang, V. Vuletić, and M. D. Lukin, Quantum nonlinear optics–photon by photon, *Nat. Photonics* **8**, 685 (2014).
- [7] Q. Li, M. Davanço, and K. Srinivasan, Efficient and low-noise single-photon-level frequency conversion interfaces using silicon nanophotonics, *Nat. Photonics* **10**, 406 (2016).
- [8] X. Lu, G. Moille, Q. Li, D. A. Westly, A. Singh, A. Rao, S.-P. Yu, T. C. Briles, S. B. Papp, and K. Srinivasan, Efficient telecom-to-visible spectral translation through ultralow power nonlinear nanophotonics, *Nat. Photonics* **13**, 593 (2019).
- [9] J.-Q. Wang, Y.-H. Yang, M. Li, X.-X. Hu, J. B. Surya, X.-B. Xu, C.-H. Dong, G.-C. Guo, H. X. Tang, and C.-L. Zou, Efficient Frequency Conversion in a Degenerate $\chi(2)$ Microresonator, *Phys. Rev. Lett.* **126**, 133601 (2021).
- [10] L. Chang, A. Boes, P. Pintus, J. D. Peters, M. Kennedy, X.-W. Guo, N. Volet, S.-P. Yu, S. B. Papp, and J. E. Bowers, Strong frequency conversion in heterogeneously integrated gaas resonators, *APL Photonics* **4**, 036103 (2019).
- [11] D. J. Wilson, K. Schneider, S. Hönl, M. Anderson, Y. Baumgartner, L. Czornomaz, T. J. Kippenberg, and P. Seidler, Integrated gallium phosphide nonlinear photonics, *Nat. Photonics* **14**, 57 (2020).
- [12] L. Chang, W. Xie, H. Shu, Q.-F. Yang, B. Shen, A. Boes, J. D. Peters, W. Jin, C. Xiang, and S. Liu, *et al.*, Ultra-efficient frequency comb generation in algaas-on-insulator microresonators, *Nat. Commun.* **11**, 1 (2020).
- [13] Z. Ma, J.-Y. Chen, Z. Li, C. Tang, Y. M. Sua, H. Fan, and Y.-P. Huang, Ultrabright Quantum Photon Sources on Chip, *Phys. Rev. Lett.* **125**, 263602 (2020).
- [14] J.-Y. Chen, C. Tang, M. Jin, Z. Li, Z. Ma, H. Fan, S. Kumar, Y. M. Sua, and Y.-P. Huang, Efficient frequency doubling with active stabilization on chip, *Laser Photonics Rev.* **15**, 2100091 (2021).
- [15] J. Lu, J. B. Surya, X. Liu, A. W. Bruch, Z. Gong, Y. Xu, and H. X. Tang, Periodically poled thin-film lithium niobate microring resonators with a second-harmonic generation efficiency of 250,000%/w, *Optica* **6**, 1455 (2019).
- [16] J.-Y. Chen, Z.-H. Ma, Y. M. Sua, Z. Li, C. Tang, and Y.-P. Huang, Ultra-efficient frequency conversion in quasi-phase-matched lithium niobate microrings, *Optica* **6**, 1244 (2019).
- [17] J. Lu, M. Li, C.-L. Zou, A. A. Sayem, and H. X. Tang, Toward 1% single-photon anharmonicity with periodically poled lithium niobate microring resonators, *Optica* **7**, 1654 (2020).
- [18] R. Gao, H. Zhang, F. Bo, W. Fang, Z. Hao, N. Yao, J. Lin, J. Guan, L. Deng, M. Wang, L. Qiao, and Y. Cheng, Broadband highly efficient nonlinear optical processes in on-chip integrated lithium niobate microdisk resonators of q-factor above 10^8 , *ArXiv:2102.00399* (2021).
- [19] V. S. Ilchenko, A. A. Savchenkov, A. B. Matsko, and L. Maleki, Nonlinear Optics and Crystalline Whispering Gallery Mode Cavities, *Phys. Rev. Lett.* **92**, 043903 (2004).
- [20] Y. Li, T. Xiang, Y. Nie, M. Sang, and X. Chen, Non-linear interaction between broadband single-photon-level coherent states, *Photonics Res.* **5**, 324 (2017).
- [21] H. Fan, Z. Ma, J. Chen, Z. Li, C. Tang, Y. Sua, and Y. Huang, Photon conversion in thin-film lithium niobate nanowaveguides: A noise analysis, *J. Opt. Soc. Am. B* **38**, 2172 (2021).
- [22] A. Singh, Q. Li, S. Liu, Y. Yu, X. Lu, C. Schneider, S. Höfling, J. Lawall, V. Verma, and R. Mirin *et al.*, Quantum frequency conversion of a quantum dot single-photon source on a nanophotonic chip, *Optica* **6**, 563 (2019).
- [23] U. Vazirani and T. Vidick, Fully device independent quantum key distribution, *Commun. ACM* **62**, 133 (2019).
- [24] J. Yang Chen, Y. M. Sua, Z. hui Ma, C. Tang, Z. Li, and Y. ping Huang, Efficient parametric frequency conversion in lithium niobate nanophotonic chips, *OSA Continuum* **2**, 2914 (2019).
- [25] J.-Y. Chen, C. Tang, Z.-H. Ma, Z. Li, Y. M. Sua, and Y.-P. Huang, Efficient and highly tunable second-harmonic generation in z-cut periodically poled lithium niobate nanowaveguides, *Opt. Lett.* **45**, 3789 (2020).
- [26] M. Jin, J.-Y. Chen, Y. M. Sua, and Y.-P. Huang, High-extinction electro-optic modulation on lithium niobate thin film, *Opt. Lett.* **44**, 1265 (2019).
- [27] Y. He, Q.-F. Yang, J. Ling, R. Luo, H. Liang, M. Li, B. Shen, H. Wang, K. Vahala, and Q. Lin, Self-starting bi-chromatic linbo 3 soliton microcomb, *Optica* **6**, 1138 (2019).
- [28] C. Wang, M. Zhang, M. Yu, R. Zhu, H. Hu, and M. Loncar, Monolithic lithium niobate photonic circuits for kerr frequency comb generation and modulation, *Nat. Commun.* **10**, 1 (2019).
- [29] M. Zhang, B. Buscaino, C. Wang, A. Shams-Ansari, C. Reimer, R. Zhu, J. M. Kahn, and M. Lončar, Broadband electro-optic frequency comb generation in a lithium niobate microring resonator, *Nature* **568**, 373 (2019).
- [30] Z. Gong, X. Liu, Y. Xu, and H. X. Tang, Near-octave lithium niobate soliton microcomb, *Optica* **7**, 1275 (2020).
- [31] J. Zhang, Y. M. Sua, J.-Y. Chen, J. Ramanathan, C. Tang, Z. Li, Y. Hu, and Y.-P. Huang, Carbon-dioxide absorption

- spectroscopy with solar photon counting and integrated lithium niobate micro-ring resonator, *Appl. Phys. Lett.* **118**, 171103 (2021).
- [32] A. Boes, B. Corcoran, L. Chang, J. Bowers, and A. Mitchell, Status and potential of lithium niobate on insulator (Inoi) for photonic integrated circuits, *Laser Photonics Rev.* **12**, 1700256 (2018).
- [33] I. Breunig, Three-wave mixing in whispering gallery resonators, *Laser Photonics Rev.* **10**, 569 (2016).
- [34] E. S. Hosseini, S. Yegnanarayanan, A. H. Atabaki, M. Soltani, and A. Adibi, Systematic design and fabrication of high-q single-mode pulley-coupled planar silicon nitride microdisk resonators at visible wavelengths, *Opt. Express* **18**, 2127 (2010).